GEOPHYSICS, VOL. 85, NO. 5 (SEPTEMBER-OCTOBER 2020); P. KS161–KS170, 11 FIGS.
10.1190/GEO2019-0667.1

Locating passive sources on seismic reflection image in the presence of velocity errors

Yujin Liu[1], Yue Ma[1], Song Han[1], and Yi Luo[2]

ABSTRACT

Locating passive-source positions by using microseismic events is essential for monitoring hydraulic fractures. Among all microseismic source locating approaches, time-reversal imaging (TRI) is a promising one that is based on the principle that all of the back-propagated receiver wavefields should coincide at the source position when the velocity is accurate. It can image microseismic sources by applying a focusing imaging condition to the reconstructed receiver wavefields. However, the TRI method is highly sensitive to velocity errors and it is time-consuming or even challenging to refine the velocity model when the subsurface structure is complex. Instead of updating the velocity model, we have adopted a new method to locate microseismic events on a seismic reflection image under the condition that the seismic data are co-located with surface or near-surface microseismic observations. This method does not correctly place the microseismic events in depth; rather, it makes them consistent with the seismic reflection image; thus, it is still capable of providing correct local structure information around the passive source without the need of building an accurate velocity model. We have theoretically analyzed the variation of the imaged source location when the velocity model is inaccurate. Our result shows that faster velocities cause shallower depths whereas slower velocities cause deeper depths of source locations on the image. This is similar to the behavior of the focusing depth, but it is opposite to that of the migration depth in active-source seismic reflection imaging. Then, we match the locations of microseismic events with the well-focused seismic reflection image, which is extracted by slicing the time-shift common-image gathers at the time lag where the image has the maximal energy. Finally, synthetic tests validate the effectiveness of the proposed approach.

INTRODUCTION

The locations of passive seismic sources induced by fluid injection during fracturing provide important information on the deformation, fluid movement, and geomechanical condition of hydrocarbon and geothermal reservoirs (Maxwell et al., 2010; Shapiro, 2015). Locating microseismic events is analogous to positioning earthquake sources in global seismology. One typical way to locate earthquakes is arrival-time inversion (Thurber and Engdahl, 2001; Pujol, 2004). However, this approach requires picking traveltimes, which can be performed either manually or automatically. For hand picking, it is tedious, labor-intensive, and time-consuming. For autopicking, it may struggle to provide reliable pickings when the wavefield is complex or the signal-to-noise ratio (S/N) is low.

One waveform-based source locating method without traveltime picking is time-reversal imaging (TRI). The basic principle of TRI methods is that the time-reversal extrapolated receiver wavefields focus at the location of seismic sources, if a reasonably accurate velocity model is given (McMechan, 1982; Gajewski and Tessmer, 2005; Fink, 2006). Based on this principle, various types of imaging conditions (ICs) have been proposed. The straightforward IC is scanning the 4D (time and 3D in space) wavefield and finding the location where it has the maximal energy. Artman et al. (2010) consider the problem of location estimation as a migration problem, and the time axis collapses by incorporating the zero-lag autocorrelation IC. Douma et al. (2013) improve the temporal and spatial focusing of a microseismic event using deconvolution. Nakata and Beroza (2016) and Sun et al. (2015) independently propose to apply

---

Manuscript received by the Editor 10 October 2019; revised manuscript received 31 May 2020; published ahead of production 21 June 2020; published online 25 September 2020.
[1]Aramco Beijing Research Center, Aramco Asia, Beijing 100102, China. E-mail: yujin.liu@aramcoasia.com (corresponding author); yue.ma@aramcoasia.com; song.han@aramcoasia.com.
[2]EXPEC Advanced Research Center, Saudi Aramco, Dhahran 31311, Saudi Arabia. E-mail: yi.luo@aramco.com.

multidimensional crosscorrelation to improve the spatial resolution of the source image produced by the zero-lag autocorrelation IC. Because the crosscorrelation IC requires wavefield propagation using data from each receiver separately, it is computationally intensive for wave-equation implementation. Sun et al. (2015) propose to apply a hybrid multiplicative TRI method to back-propagated wavefields computed from groups of receivers to mitigate this cost problem. Zhu et al. (2019) further detail the implementation of the hybrid multiplicative TRI method and show the failure of the crosscorrelation IC in the presence of strong noise, but the hybrid IC works satisfactorily. Sun et al. (2016) show that the time-reversal wavefield does not provide accurate amplitude and phase information of the passive source function because the time-reversal wavefield is modeled by the adjoint-state equation, not exactly the inverse of the forward wave propagation. This problem can be addressed by the waveform-inversion method (Sun et al., 2016). The spatial resolution of the source image can be further improved by adding a regularization term in the objective function of the waveform-inversion method to impose sparsity in space and smoothness in time on the source wavefield (Gao et al., 2017; Sharan et al., 2018; Li et al., 2019).

All of the above TRI methods require an accurate velocity model. Errors in the velocity model may lead to mislocations of microseismic events. A practical way to construct a velocity model is spatial interpolation of the 1D laterally homogeneous velocity model from sonic logs or vertical seismic profile check shots. Another way to obtain a reliable velocity model is inverting for the velocity model and the microseismic location simultaneously. For example, Li et al. (2013) use differential arrival times and differential backazimuths to better constrain microseismic locations and the anisotropic model; Zhang et al. (2017, 2018) apply Bayesian inference for simultaneous inversion of multiple microseismic data to obtain event locations along with the subsurface velocity model. A more complex model could be developed to include topographic elevation changes to the layers, based on a geologic structural model or seismic horizons. Alternately, a full 3D velocity model could be constructed if sufficient information exists to quantify lateral velocity changes. Recently, much effort has been put into estimating the velocity model using passive seismic waveform data. Sun et al. (2016) propose a waveform-based framework for joint inversion with passive seismic source functions and velocities. Song et al. (2019) introduce a source-focusing function as an additional objective function to optimize the velocity model and source image. Their method is less vulnerable to cycle-skipping problems compared to conventional full-waveform inversion. Witten and Shragge (2015, 2017) devise a multidimensional extended IC for passive seismic imaging and evaluate the focusing of the extended PS image volume to update compressional-wave (P-wave) and shear wave (S-wave) velocities. Similarly, Nakata (2018) extends the multidimensional crosscorrelation IC (Sun et al., 2015; Nakata and Beroza, 2016) to identify the signatures of velocities errors in this domain. However, due to the inadequate data acquisition and noises in the data, the seismic velocity inversion is inherently nonunique. Therefore, the inverted velocity model generally is required to be adjusted and validated using calibration shots (sources with known locations; Maxwell et al., 2010), including perforation shots or sleeve-opening events recorded during hydraulic fracturing (Eaton, 2018). Due to the noisy environment associated with hydraulic fracturing activities, it is sometimes challenging to detect calibration shots using a surface or near-surface geophone array (Chambers et al., 2010). In the case of microseismic data recorded by broadband regional seismograph networks, calibration shots are hardly recognizable; thus, the focal depth has great uncertainties (Schultz et al., 2017).

If a colocated seismic volume is available, determining the relative locations of microseismic events within a seismic image is as important as estimating their absolute locations for the purpose of interpretation. Several studies have used double-difference and/or waveform crosscorrelation methods to obtain accurate relative hypocenter locations for induced seismic events (Skoumal et al., 2015; Bao and Eaton, 2016; Schoenball and Ellsworth, 2017). The double-difference algorithm reduces the impact of velocity-model uncertainty through the use of groups of events with similar source-receiver raypaths (Waldhauser and Ellsworth, 2000). Although this approach often yields small uncertainties in terms of relative hypocenter locations, it does not reduce the uncertainty in the absolute location unless calibration events with known locations are available (Eaton, 2018). Poulin et al. (2019) propose a focal-time analysis method to obtain robust stratigraphic depth control for microseismicity without building an accurate velocity model. The basic principle is that the difference in the P- and S-arrival times of microseismic events could be registered to the zero-offset PP reflection time (or the focal time) by searching the lookup table constructed through the correlation of PP and PS reflection times. This method is demonstrated to provide relatively accurate stratigraphic depth control for induced events. However, it requires multicomponent seismic data that might be unavailable in conventional seismic acquisition. Furthermore, it needs to pick P- and S-arrival times of microseismic events and correlate (register) equivalent marker reflections that are clearly discernible and could be accurately picked in the PP and PS seismic volumes. Picking is usually one of the main factors that introduces uncertainties for estimating the locations of microseismic events (Eisner et al., 2009).

In this paper, we propose a new waveform-based approach that does not require traveltime picking for determining the relative locations of microseismic events within a seismic image. This method relies on joint processing of passive- and active-seismic data; therefore, it is limited in its application to areas where both surveys are colocated. Nevertheless, this method only needs P-wave data, and it eliminates the necessity to build an accurate velocity model for microseismic source locating. To achieve this goal, we first analyze the variation of TRI imaged source locations with respect to velocity errors and derive an analytical formula to describe the relation of imaged source locations to migration velocity under the far-field approximation. Then, we propose to use a well-focused seismic reflection image to register the source location provided by TRI methods. Finally, two synthetic tests are used to verify the source location formula and demonstrate the potential of the proposed source registration method.

THEORY

First, we briefly review the methodology of the TRI methods, and then we derive an analytical formula of the imaged source locations with respect to velocity errors. Finally, we propose an approach to locate the microseismic events on the active-source seismic reflection image in the presence of velocity errors.

Time-reversal imaging

The TRI principle states that all of the wavefields back propagating in time from receivers coincide at the correct source location when the velocity is accurate. In the frequency domain, the back-propagation of recorded seismic data can be written as

$$U(\mathbf{x},\omega)=\sum_{i=1}^{N}G^{*}(\mathbf{x}_{r_i},\mathbf{x},\omega)D(\mathbf{x}_{r_i},\omega), \tag{1}$$

where $\mathbf{x}$ is the spatial coordinate, ω is the angular frequency, N is the number of receivers, and $\mathbf{x}_{r_i}$ is the location of the ith receiver. The expression $D(\mathbf{x}_{r_i},\omega)$ is the observed data on the ith receiver, and $G^{*}(\mathbf{x}_{r_i},\mathbf{x},\omega)$ is the Green's function representing an impulse response observed at the receiver $\mathbf{x}_{r_i}$ due to a source at $\boldsymbol{x}$. For wave-equation extrapolation, the observed data at all receivers are back-propagated simultaneously; thus, the summation in the above equation is computed implicitly. The source image can be extracted from the reconstructed wavefield $U(\mathbf{x},\omega)$ by applying an IC,

$$I(\mathbf{x})=U(\mathbf{x},\omega)_{\mathrm{IC}}, \tag{2}$$

where $\cdot_{\mathrm{IC}}$ denotes the IC. Among various ICs, one option is searching for a focusing point with the maximal amplitude through the time axis, which can be expressed as

$$t_0=\underset{t}{\operatorname{argmax}}\,u(\mathbf{x},t), \tag{3}$$

where $u(\mathbf{x},t)$ is the inverse Fourier transform of $U(\mathbf{x},\omega)$. The resulting source image is

$$I(\mathbf{x})=u(\mathbf{x},t_0). \tag{4}$$

This method is briefly called direct TRI (D-TRI) in the following section.

To introduce other variants of TRI methods, we take two wavefields back-propagated from the recorded data at the ith and jth receivers as an example. The principle of TRI states that these two wavefields should coincide at the correct source location; thus, the zero-lag crosscorrelation results of them will yield a source image if the velocity is accurate (Claerbout, 1971), that is,

$$I_{ij}(\mathbf{x})=\sum_{\omega}U^{*}_{r_i}(\mathbf{x},\omega)U_{r_j}(\mathbf{x},\omega), \tag{5}$$

where the two receiver wavefields can be expressed as

$$U_{r_k}(\mathbf{x},\omega)=G^{*}(\mathbf{x}_{r_k},\mathbf{x},\omega)D(\mathbf{x}_{r_k},\omega),\, k=i,j. \tag{6}$$

Images constructed by different pairs of (r_i,r_j) provide the same source image but with different migration artifacts. One straightforward way to suppress these artifacts is by calculating the average (or arithmetic mean) image of all of the receiver pairs, that is,

$$I(\mathbf{x})=\sum_{i=1}^{N}\sum_{j=1}^{N}\sum_{\omega}U^{*}_{r_i}(\mathbf{x},\omega)U_{r_j}(\mathbf{x},\omega). \tag{7}$$

After interchanging the summation orders and transforming equation 7 to the time domain, we have

$$I(\mathbf{x})=\sum_{t}\left(\sum_{i=1}^{N}u_{r_i}(\mathbf{x},t)\right)^{2}, \tag{8}$$

where $u_{r_i}(\mathbf{x},t)$ is the inverse Fourier transform of $U_{r_i}(\mathbf{x},\omega)$. This is the zero-lag autocorrelation IC (AC-TRI) proposed by Artman et al. (2010).

Another way to suppress the artifacts is taking the multiplication (or geometric-mean) of all of the receiver wavefield pairs (Sun et al., 2015; Nakata and Beroza, 2016), that is,

$$I(\mathbf{x})=\sum_{t}\prod_{i=1}^{N}u_{r_i}(\mathbf{x},t). \tag{9}$$

As opposed to AC-TRI, in which the entire data volume is back-propagated at once, equation 9 has to be carried out by back-propagation from each receiver, leading to a huge increase in the computational cost for wave-equation implementation. To improve the efficiency, Sun et al. (2015) propose to divide the data into different groups and then back-propagate each group before applying the geometric-mean IC. We call this technique hybrid multiplicative TRI (HM-TRI). The imaging step is thus replaced by

$$I(\mathbf{x})=\sum_{t}\prod_{i=1}^{n_g}\sum_{j=1}^{n_i}u_{r_{(i-1)\times n_i+j}}(\mathbf{x},t), \tag{10}$$

where n_g is the total number of groups and n_i is the number of receivers in the ith group; thus, $\sum_{i=1}^{n_g}n_i=N$.

All of the above focusing ICs (D-TRI, AC-TRI, and HM-TRI) are based on the same principle in that the back-propagated wavefields should coincide at the correct source position and at the correct initiation time, as stated by equation 5 if only two wavefields are considered. After rearranging equation 5, we obtain

$$I_{ij}(\mathbf{x})=\sum_{\omega}G(\mathbf{x}_{r_i},\mathbf{x},\omega)G^{*}(\mathbf{x}_{r_j},\mathbf{x},\omega)D^{*}(\mathbf{x}_{r_i},\omega)D(\mathbf{x}_{r_j},\omega), \tag{11}$$

where the first two terms constitute the migration kernel (Schuster et al., 2004) and the last two terms calculate the crosscorrelation of the two traces at $\mathbf{x}_{r_i}$ and $\mathbf{x}_{r_j}$. If we only consider the first arrivals and ignore the amplitude information of these two traces, the crosscorrelation can be regarded as calculating the traveltime difference from the source $\mathbf{x}$ to the receivers at $\mathbf{x}_{r_i}$ and $\mathbf{x}_{r_j}$. Meanwhile, the migration kernel can be simplified as

$$K(\mathbf{x},\mathbf{x}_{r_i},\mathbf{x}_{r_j},\omega)=e^{i\omega[t(\mathbf{x}_{r_j},\mathbf{x})-t(\mathbf{x}_{r_i},\mathbf{x})]}, \tag{12}$$

where $t(\mathbf{x}_{r_i},\mathbf{x})$ and $t(\mathbf{x}_{r_j},\mathbf{x})$ are the traveltime from the source $\mathbf{x}$ to the receivers at $\mathbf{x}_{r_i}$ and $\mathbf{x}_{r_j}$, respectively. The migration kernel annihilates the traveltime difference $t(\mathbf{x}_{r_j},\mathbf{x})-t(\mathbf{x}_{r_i},\mathbf{x})$, when the trial source location $\mathbf{x}$ is at the true place.

Variation of imaged source locations with respect to velocity errors

Consider an underground source and two receivers at the surface, as shown in Figure 1. The term s denotes the source located at (x,z). The terms r_i and r_j are the locations of these two receivers. The midpoint of r_i and r_j is ξ, and the half distance between r_i and r_j is h. Assuming that the velocity above s is constant v, and the traveltime difference between the raypaths of sr_j and sr_i is τ, then this traveltime difference satisfies

$$\tau = \frac{1}{v}\left[\sqrt{(\xi - x + h)^2 + z^2} - \sqrt{(\xi - x - h)^2 + z^2}\right]. \quad (13)$$

Under the far-field assumption that $\xi - x + h \ll z$ and $\xi - x - h \ll z$, we can expand the two square roots in equation 13 using the Taylor approximation and consider the first-order term only, leading to

$$\tau = \frac{2(\xi - x)h}{vz}. \quad (14)$$

Given the migration velocity v_m, the locus of all possible source locations is defined by the following equation:

$$\tau = \frac{2(\xi - x_m)h}{v_m z_m}, \quad (15)$$

where (x_m, z_m) defines the domain of the imaged source locations. Substituting equation 14 into equation 15, we have

$$F(x_m, z_m; \xi) = z_m\beta(\xi - x) - z(\xi - x_m) = 0, \quad (16)$$

where $\beta = v_m/v$. This is essentially a straight line in the image space (x_m, z_m) for this special case of constant velocity and far-field approximation. The final image of all of these traveltime differences calculated from many receiver pairs is the envelope of the individual straight lines. The envelope of these straight lines is the solution of equation 16 and its derivative equation:

$$F_\xi(x_m, z_m; \xi) = z_m\beta - z = 0. \quad (17)$$

Solving equations 16 and 17, we obtain

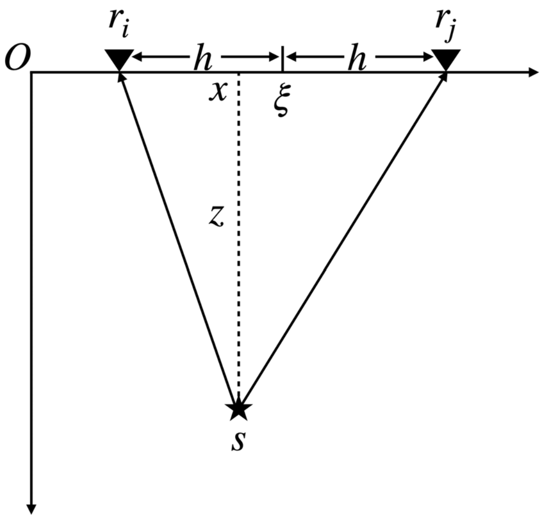

Figure 1. Geometry for a subsurface source s at (x, z). Two receivers r_i and r_j are at the surface. The middle point and the half distance of these two receivers are ξ and h, respectively.

$$x_m = x, \quad (18)$$

$$z_m = \frac{z}{\beta}. \quad (19)$$

From equations 18 and 19, we observe that, under the far-field approximation ($\xi - x + h \ll z$ and $\xi - x - h \ll z$), the lateral position of the imaged source is invariant whereas the depth position of the imaged source shifts when the velocity is inaccurate. More specifically, in the case of the migration velocity being smaller than the medium velocity, that is, $\beta < 1$, the imaged source location is deeper than the true one; in the case of the migration velocity being greater than the medium velocity, that is, $\beta > 1$, the imaged source location is shallower than the true one.

Locating passive sources on seismic reflection images

In this section, we first introduce two different seismic images computed from seismic reflection data and outline their behavior of depth variation with respect to velocity errors. Then, we justify the use of one of these two images within which to locate passive sources, so that the imaged sources and seismic image are self-consistent.

The first image is a traditional one that can be obtained by the zero-time IC for shot-profile depth migration. This IC consists of time crosscorrelation at every image location between the source and receiver wavefields, followed by image extraction at zero time. It can be expressed in the frequency domain as

$$M(\mathbf{x}) = \sum_\omega W_s^*(\mathbf{x}, \omega)W_r(\mathbf{x}, \omega), \quad (20)$$

where $M(\mathbf{x})$ denotes this migrated image, $W_s(\mathbf{x}, \omega)$ is the source wavefield obtained by forward propagating the active source at the surface, and $W_r(\mathbf{x}, \omega)$ is the receiver wavefield obtained by back propagating the seismic data recorded at the surface. The depth coordinate of this migrated image is often called the migration depth. Many studies demonstrate that faster velocities cause a deeper migration depth whereas slower velocities cause a shallower migration depth (for example, Zhu et al., 1998).

The second seismic image is a well-focused image that can be extracted from the time-shift IC for shot-profile depth migration. This IC involves shifting of the source and receiver wavefields in time, followed by image extraction at zero time (Sava and Fomel, 2006). It can be expressed in the frequency domain as

$$M(\mathbf{x}, \epsilon) = \sum_\omega W_s^*(\mathbf{x}, \omega)W_r(\mathbf{x}, \omega)e^{i\omega\epsilon}, \quad (21)$$

where ϵ is a scalar that describes the time-shift between the source and receiver wavefields before imaging. After generating the time-shift common-image gather using equation 21, the well-focused image can be obtained by picking the focus point with the maximal energy for each reflection event in the common-image gather (Wang et al., 2009), that is

$$M_{\text{focus}}(\mathbf{x}) = M(\mathbf{x}, \epsilon_0), \quad (22)$$

where ϵ_0 is the picked time shift as a function of $\mathbf{x}$. The depth coordinate of this migrated image is often called the focusing depth.

MacKay and Abma (1992) show that faster velocities cause a shallower focusing depth whereas slower velocities cause a deeper focusing depth. Moreover, they have proven that, under the assumption of the far-field approximation, the focusing depth z_{focus} has the following relationship with respect to velocity errors:

$$z_{\mathrm{focus}} = \frac{z}{\beta}. \tag{23}$$

Compared to equation 19, the behavior of the imaged source location with respect to velocity errors is exactly the same as that of the focusing depth, but is opposite to that of the migration depth in seismic reflection imaging. Therefore, under the assumptions of the far-field approximation, we can use the well-focused seismic reflection image to match the passive source location.

In other words, by using the well-focused seismic reflection image, we can provide correct reflector information around the microseismic source locations even though the velocity is incorrect. Hence, instead of updating the velocity model and finding the accurate absolute locations of microseismic events, we propose to make the relative locations of microseismic events consistent with the seismic reflection image, or more specifically, the well-focused seismic image obtained from slicing the time-shift common-image gathers.

Before locating the passive source on seismic reflection image, we first need to preprocess the synthetic passive- and active-source data. Because we only consider making the P-wave source location consistent with the PP reflection image in this paper, it is necessary to extract the P-waves from the raw data in advance. For the passive-source data, we apply a mask around the direct P-wave arrivals in the vertical-component data. If there is a polarity reversal problem in the extracted P-wave event, we further double the phase component of the analytical signal for each trace. By doubling the instantaneous phase, we remove the polarity reversals ensuring that the resultant stack or sum of the model-aligned signals will add constructively and at the correct location (Drew et al., 2014). For the active-source data, we also need to extract the P-wave information from the vertical-component data. It has been demonstrated that effective P- and S-wave separation can be achieved using vector rotation (Wang et al., 2002), *f*-*k* filtering (Li et al., 2015), wavefield extrapolation (Sun et al., 2004), and reciprocity between sources and receivers (Huang and Milkereit, 2007); however, discussion of the merits of these methods is beyond the scope of this article. For the sake of simplicity, in the following numerical examples, we apply Helmholtz decomposition during the simulation to obtain clean P-wave potential data. In addition, the direct P-wave should be muted before seismic reflection imaging.

RESULTS

In this section, two synthetic tests are used to validate the proposed approach that registers the source location on the seismic reflection image. The first model consists of a horizontal reflector embedded in a two-layer velocity medium. The second model consists of an anticline and several dipping reflectors embedded in a complex velocity medium.

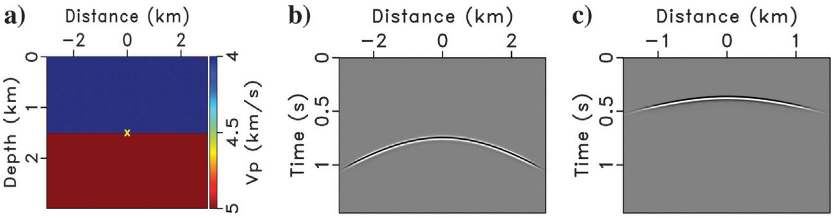

Figure 2. (a) A two-layer velocity model. The yellow cross indicates the location of the passive source. The receivers are deployed at the surface. (b) Recorded data from an active source at 0 km at the surface. (c) Recorded data from the passive source.

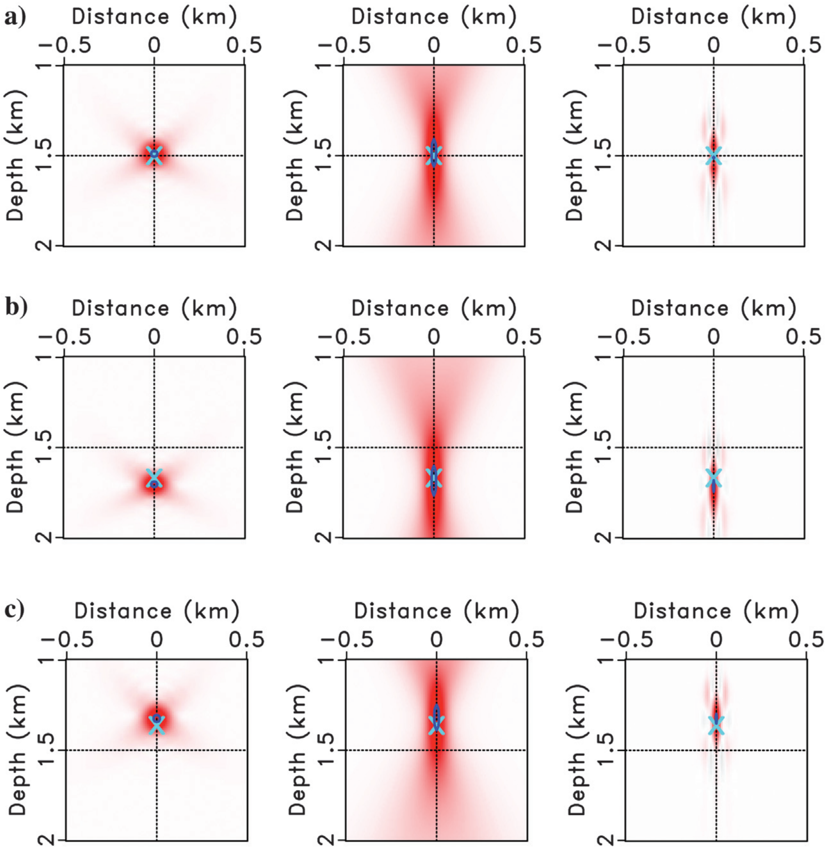

Figure 3. Source images of the D-TRI, AC-TRI, and HM-TRI methods using the (a) correct, (b) 10% lower, and (c) 10% higher velocities. The D-TRI images are in the left column. The AC-TRI images are in the middle column. The right column shows the HM-TRI images. The blue ring in each image displays a contour with $I(\mathbf{x}) = 0.95$ after image normalization. The cyan cross in each image shows the predicted location calculated by the analytical solution.

Constant velocity model

Figure 2a shows the velocity model, which contains two layers with top and bottom velocities equal to 4 and 5 km/s, respectively. The active source is located at the surface with the horizontal axis equal to 0 km, and the passive source is located at the position (0, 1.5) km, shown as a yellow cross in Figure 2a. There are two slightly different acquisition systems to record the signals from the active and passive sources. The active-source acquisition system has 600 receivers deployed from −3 to 3 km at the surface with a spatial interval of 0.01 km, and the passive-source acquisition system has 300 receivers deployed from −1.5 to 1.5 km at the surface with a spatial interval of 0.01 km. The active and passive source functions are Ricker wavelets with a peak frequency of 30 Hz. Figures 2b and 2c show two records stimulated by the active and passive sources, respectively.

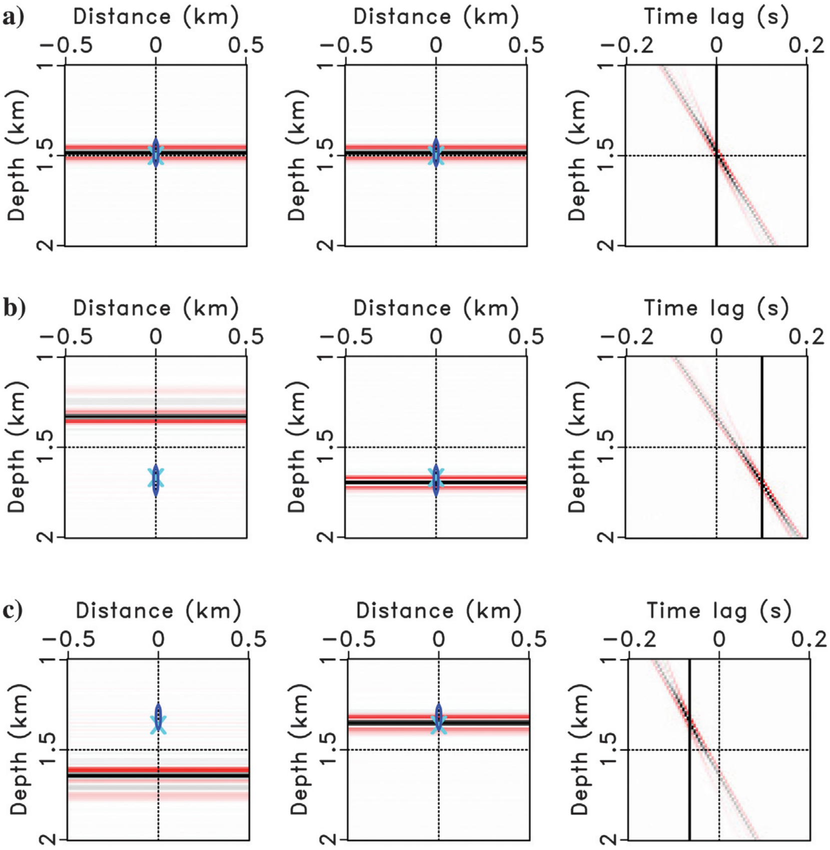

Figure 4. Source locations overlaid on the seismic reflection images using the (a) correct, (b) 10% lower, and (c) 10% higher velocities. The left column is the seismic reflection image using zero-time IC, the middle column is the well-focused seismic reflection image extracted from the time-shift common-image gather shown in the right column, where the black line indicates the picked time lag for extracting the well-focused image. The blue rings in the images show contour with $I(\mathbf{x}) = 0.95$ in the AC-TRI images. The cyan crosses in the images show the predicted location calculated by the analytical solution.

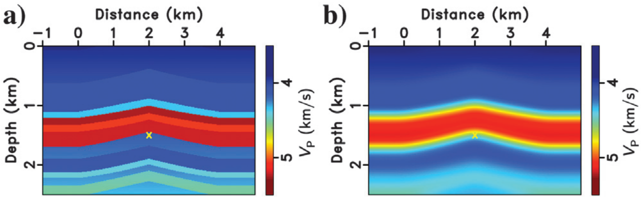

Figure 5. (a) The P-wave velocity model for elastic simulation. (b) Smoothed P-wave velocity model for passive source locating and active-source seismic reflection migration. A constant density model $\rho = 2500\ \mathrm{kg/m^3}$ and a constant $V_P/V_S = 2$ are used. The yellow cross indicates the passive source location. The receivers are deployed at the surface to record signals from passive- and active sources.

We apply the D-TRI, AC-TRI, and HM-TRI methods to locate the microseismic event using different velocities. The results are shown in Figure 3. For the HM-TRI method, we divide the data into six groups by index order. Each group involves 50 neighboring traces. In Figure 3, it is obvious that the HM-TRI has the highest resolution whereas the AC-TRI method has the lowest resolution. To illustrate the resolution difference of these TRI source locating methods, we normalize each source image and overlay the contour of $I(\mathbf{x}) = 0.95$ in a blue ring. To verify the accuracy of the derived analytical solution (equations 18 and 19), we also overlay the predicted location in the cyan cross. Compared to the imaged and theoretical source locations, we can observe that the analytical formula describes the behavior of the imaged source location quite well in this example, even though the derivation is based on the far-field approximation.

To validate the proposed locating approach, we overlay the contour display and the theoretical location on the reflector images obtained from the active-source seismic data. Depth migration with zero-time IC provides correct reflector information surrounding the source image in the case of a correct velocity. However, it fails to provide correct reflector information when the velocity is incorrect, as shown in the left column of Figure 4. To match the source location and reflector location correctly, we scan the time-shift common-image gathers and pick the focus, that is, the maximal energy, for all of the reflectors. The resulting image is shown in the middle column of Figure 4. Compared with the normal depth image using the zero-time IC, the well-focused depth image using non-zero time IC provides correct reflector information around the source location regardless of having correct or incorrect velocities. The right column of Figure 4 shows the time-shift common-image gathers overlaid with black curves picked for the well-focused images in the middle column.

Complex velocity model

In this section, we use a complex synthetic example to test the proposed method. Figures 5a and 5b show the P-wave velocity model for elastic simulation and for migration, respectively. The S-wave velocity model for elastic simulation is a scaled version of the P-wave velocity shown in Figure 5a, with a fixed ratio of

$V_P/V_S = 2$. We use a constant density model of $\rho = 2500\ \mathrm{kg/m^3}$ for the simulation and the migration. The passive- and active-source data are simulated using a space-time staggered-grid finite-difference solution to the isotropic elastic wave equation (Virieux, 1984, 1986). For passive-source simulation, we place a horizontal double-couple point source at (2.0, 1.5) km to simulate microseismic events induced by hydraulic fracturing. As indicated by the yellow cross in Figure 5a, the passive source is located just below the anticline in the model. The horizontal double-couple source mechanism is modeled by seeding the xz component of the stress tensor with a source wavelet (Aki and Richards, 2002; Artman et al., 2010). There are 100 receivers with a spatial interval of 0.04 km from 0 to 4 km at the surface to record the vertical component of the wavefield displacement from the passive source, as shown in Figure 6a. Due to the effect of the passive source mechanism, the polarity of the P- and S-waves changes over the receiver array. At the same time, simulate 100 explosive sources at the surface with a spatial interval of 0.04 km and we place 600 receivers at the surface with spacing of 0.01 km to record the vertical component of wavefield displacement. The sources and receivers are evenly distributed from −1 to 5 km at the surface. The vertical component of a common-shot gather with the shot located at $x = 2$ km is shown in Figure 6b. The passive- and active-source time functions used here are the same Ricker wavelet of 15 Hz central frequency.

Figure 6c shows the preprocessed passive data after applying a mask around the direct P-wave event and doubling its instantaneous phase. Compared with the raw vertical-component data shown in Figure 6a, the preprocessed data mainly contain direct P-wave energy and have no polarity reversal problem. Figure 6d shows one of the preprocessed active-source common-shot gathers after applying Helmholtz decomposition during the simulation and muting of the direct P-wave. Compared with the raw vertical-component data shown in Figure 6b, the preprocessed active-source data mostly contain PP reflected waves.

Then, we apply the D-TRI, AC-TRI, and HM-TRI methods to the preprocessed passive data for source location with correct, 10% lower, and 10% higher velocities. For the HM-TRI method, we divide the data into eight groups by index order and each group involves 50 neighboring traces. The D-TRI, AC-TRI, and HM-TRI source images are shown in Figures 7a–7c, respectively. To illustrate the resolution differences, we also normalize each source image and overlay the contour with $I(\mathbf{x}) = 0.9$ in a blue ring. Comparing these three images, we observe that the HM-TRI source image has the highest resolution. Moreover, it is also obvious that these three images share a very similar variation of source location with respect to velocity errors; that is, faster velocities cause a shallower depth whereas slower velocities cause a deeper depth of the source location.

We also apply prestack depth migration to obtain reflection images with correct, 10% lower, and 10% higher velocities. To register the located source on these reflector images, we overlay the contour displays of source images on the reflection images. Because the D-TRI, AC-TRI, and HM-TRI

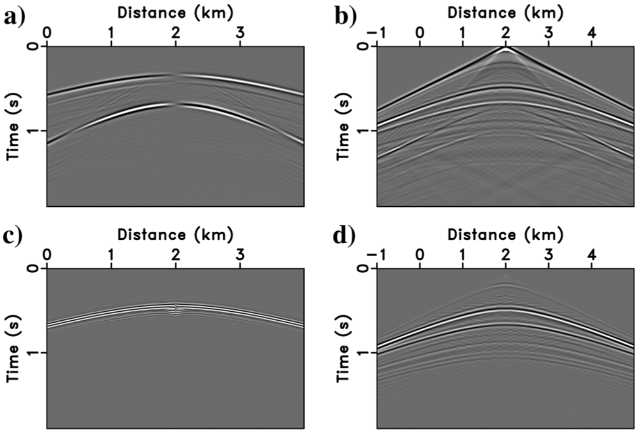

Figure 6. Modeled vertical data components from (a) the subsurface passive source and (b) an active source at the surface $x = 2$ km. (c and d) Preprocessed results of (a and b), respectively.

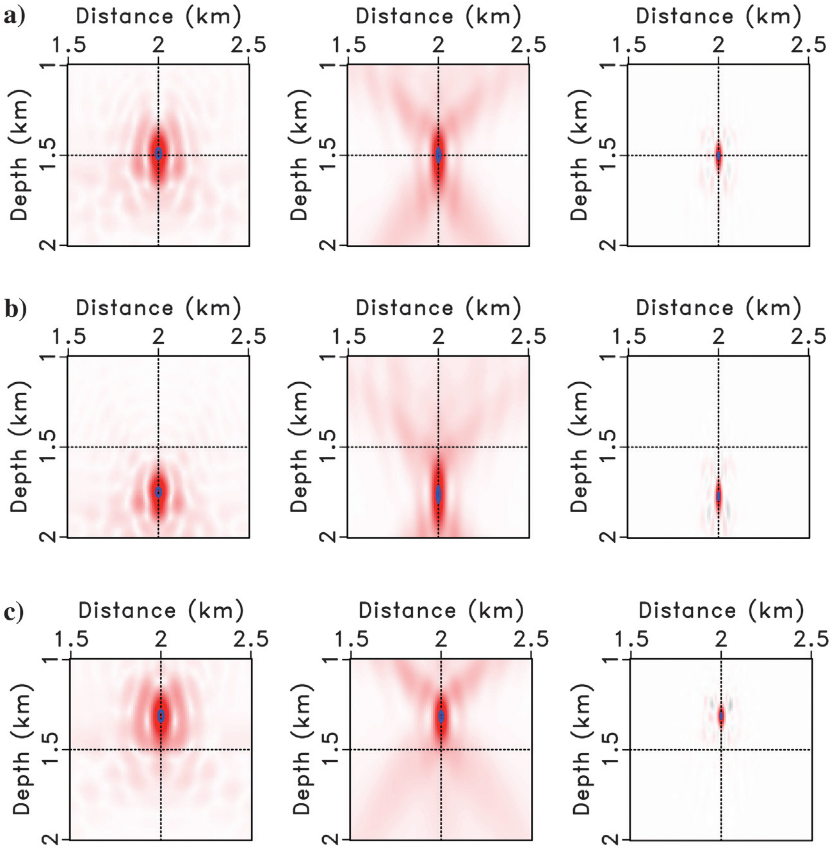

Figure 7. Source images with the D-TRI, AC-TRI, and HM-TRI methods using the (a) correct, (b) 10% lower, and (c) 10% higher velocities. The left column is the TRI image, the middle column is the AC-TRI image, and the right column is the HM-TRI image. The intersection point of the dashed lines in each image indicates the true source location. The blue ring in each image is the contour with $I(\mathbf{x}) = 0.9$ after image normalization.

methods provide almost the same source location, only the AC-TRI results are used for relative location registration. As can be observed from Figure 8, prestack depth migration with zero-time IC provides correct reflector information surrounding the source image in the case of correct velocity. However, it fails to provide correct reflector information when the velocity is incorrect, as is evident in the left column of Figure 8. To match the located source with imaged reflectors correctly, we pick the time lag in the time-shift common-image gathers with the most focusing energy and then extract the well-focused image from the common-image gathers. The matching results are shown in the middle column of Figure 8. Compared with the depth images generated by the zero-time IC, the well-focused depth images generated by the non-zero-time IC provide the correct reflector image around the source location even when the velocity is not accurate. The right column of Figure 8 shows time-shift common-image gathers at $x = 2$ km overlaid with picked time lags indicated by the black curves.

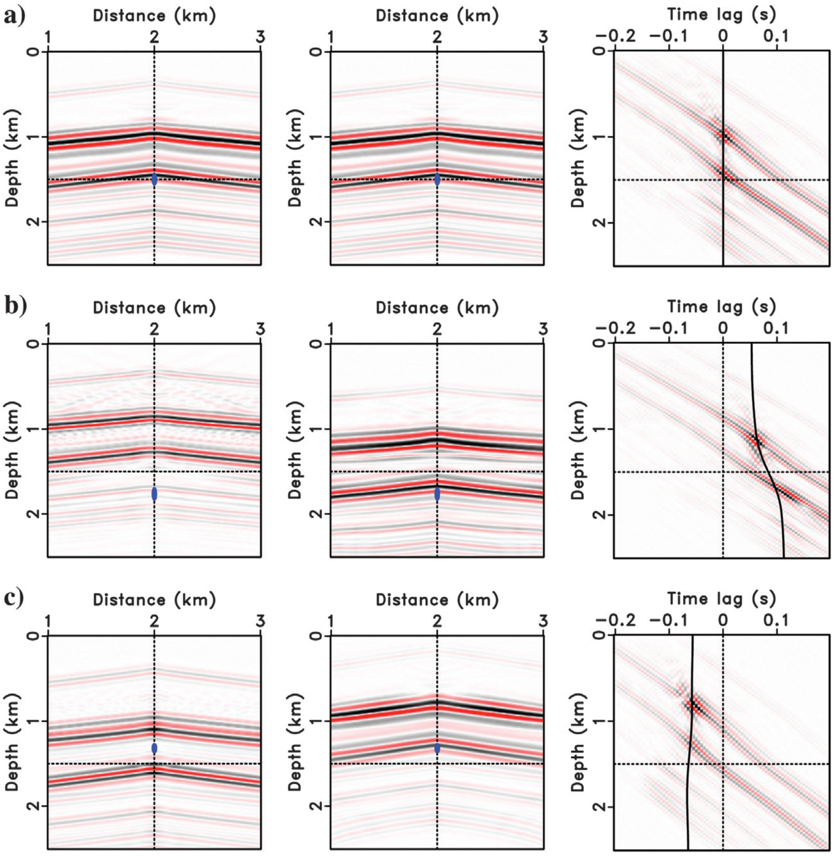

Figure 8. Source locations overlaid on the seismic reflection images using the (a) correct, (b) 10% lower, and (c) 10% higher velocities. The left column is the seismic reflection image with zero-time IC, the middle column is the well-focused seismic reflection image, and the right column is the time-shift common-image gather, where the black line indicates the picked time lag for extracting the well-focused image. The blue rings in the images show contour with $I(\mathbf{x}) = 0.9$ in the AC-TRI images.

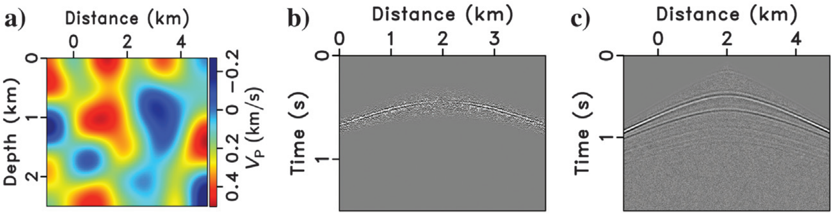

Figure 9. (a) The difference between the true background velocity in Figure 5b and the background velocity used for passive source location and active-source reflection imaging. (b) The preprocessed passive-source data. (c) The preprocessed active-source common-shot gather at the surface $x = 2$ km.

Finally, we test the proposed method using noisy data and non-uniform velocity errors. Figure 9a shows the difference between the accurate background velocity model (Figure 5b) and the background velocity model that we use for the following passive source locating and active-source reflection imaging. The velocity error shown in Figure 9a is computed by smoothing a random velocity model. We add different amounts of noise to the passive- and active-source data. The S/Ns of the passive- and active-source data are −18.25 and −12.2 dB, respectively. This is reasonable because the passive source is often much weaker than the active source. Figures 9b and 9c show the preprocessed passive- and active-source data, in which the passive data mainly contain the direct P-wave and the active-source data mainly contain PP reflected waves. The preprocessing workflow here is the same as that used in the previous noise-free data preprocessing.

Figures 10a–10c show the source images computed using the D-TRI, AC-TRI, and HM-TRI methods with the erroneous background velocity model with the errors shown in Figure 9a. Compared to the true source location indicated by the intersection of the dashed lines, the imaged location shifts to the upper right due to the overall inhomogeneous faster velocities. It is also obvious that the HM-TRI image has the highest resolution among these three images even when the data have a low S/N, which has also been well demonstrated by Zhu et al., (2019). Figure 11 shows the source registration results using the prestack depth migration image. As expected, the reflection image obtained by the zero-lag IC cannot provide correct reflector information around the imaged source. However, the well-focused reflection image picked from the time-shift common-image gathers is capable of providing the correct reflector information even though the velocity error is highly inhomogeneous. Thus, it demonstrates that the proposed method has great potential to correctly place the passive source on the migrated image even in complex geologic settings.

DISCUSSION

We have proposed a new approach to register passive source locations on the active-source seismic reflection image when the velocity is

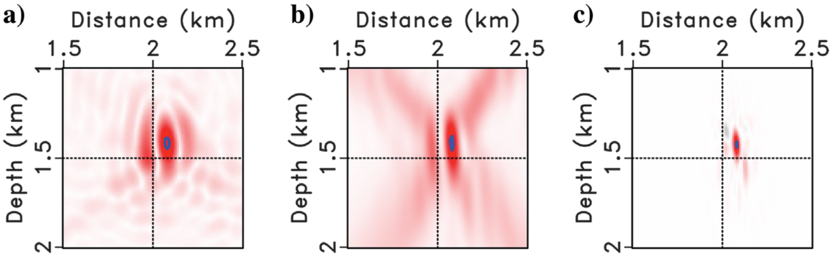

Figure 10. Source images computed by the (a) D-TRI, (b) AC-TRI, and (c) HM-TRI methods using the background velocity with the errors shown in Figure 9a. The blue ring in each image is the contour with $I(\mathbf{x}) = 0.9$ after image normalization.

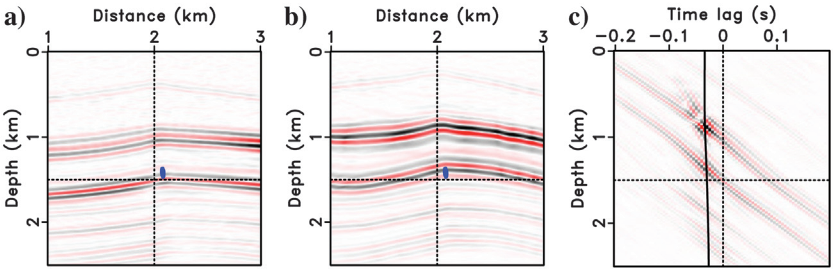

Figure 11. Source locations overlaid on the seismic reflection images using the background velocity with the errors shown in Figure 9a. The seismic reflection images are obtained by (a) the zero-time IC and (b) picking the well-focused image from the time-shift common-image gathers. One of the time-shift common-image gathers is shown in (c). The blue rings in the images show the contour with $I(\mathbf{x}) = 0.9$ in the AC-TRI images. The black line in panel (c) indicates the picked time lag for extracting the well-focused image.

not accurate. This approach is capable of providing the correct reflector image around the source locations without optimizing the velocity model, but at the cost of generating time-shift common-image gathers from the active-source seismic reflection data. Even though the synthetic tests demonstrate its potential in relatively placing microseismic events on the migrated image for a complex model, there is no theoretical guarantee when the assumption of constant velocity and the far-field approximation is not satisfied. Therefore, the ultimate solution is still improving the velocity model. In fact, the derived analytical formula of imaged source locations with respect to velocity errors also can be used for velocity updating, similar to the depth-focusing analysis proposed by MacKay and Abma (1992) in active-source seismic reflection imaging. This subject is beyond the scope of this paper and remains to be explored in the near future.

It is worth noting that, similar to the focal-time analysis method (Poulin et al., 2019), the proposed method requires colocated seismic data so that the microseismic source location can be made consistent with the well-focused seismic image. Therefore, this method is primarily suited for use with passive-seismic data acquired using a surface or near-surface sensor array, rather than a downhole system. However, our method does not require multicomponent seismic data that are often unavailable in most exploration areas; thus, it might be applicable in the field with fewer limitations than the focal-time analysis method.

Although the passive-seismic and seismic-reflection data are initially processed using two parallel workflows that merge at the end, the common processing methods that might affect the microseismic arrival times and reflection times should share the same parameters, such as the statics and the attenuation factor. In principle, the wavefields for source locating and reflection imaging should be reconstructed by the same wave extrapolation operator no matter if the operator is derived in acoustic, viscoacoustic, or anisotropic media. Under these conditions, the proposed method even with acoustic propagator is capable of accounting for factors that are often poorly constrained for most microseismic velocity models, for instance, seismic anisotropy of the medium because these factors similarly affect the microseismic arrival times and reflection times. However, the inference of phases other than the single direct P-wave has not been investigated during the source imaging and will be studied in the future.

We emphasize that picking the time lag where the seismic reflection image has maximal energy is extremely important for our approach because the time lag determines which reflection image from the time-shift common-image gathers will be used to register the source location. Therefore, the picking process should be implemented carefully.

CONCLUSION

We have derived an analytical formula of imaged source locations with respect to velocity errors. It shows that, if the migration velocity is slower than the medium velocity, the imaged source location becomes deeper than the true one; if the migration velocity is faster than the medium velocity, the imaged source location becomes shallower than the true one. This behavior is opposite to that of the migration depth, but the same as that of the focusing depth, in seismic reflection imaging. We further demonstrate that the formula of imaged source locations with respect to velocity errors is exactly the same as the depth-focusing relationship of the seismic reflection image under the assumption of constant velocity and the far-field approximation. Thus, we propose to locate the passive sources on the well-focused seismic reflection image extracted from the time-shift common-image gather. This approach works well in the presence of velocity errors without the need for updating the velocity model. Synthetic examples verify the derived analytical formula of the imaged source locations with respect to velocity errors and validate that the proposed approach is effective even in a complex medium. Our results suggest that there may be considerable value to the industry for time-shift common-image gathers to be used more routinely in the joint processing of hydraulic fracturing data sets.

ACKNOWLEDGEMENTS

The authors thank Saudi Aramco for the permission to publish this paper. We appreciate the inspiring discussion with our colleagues A. Bakulin and I. Silvestrov. We thank the editor-in-chief J. Shragge, associate editor B. Witten, and two anonymous reviewers for their valuable suggestions.

DATA AND MATERIALS AVAILABILITY

Data associated with this research are available and can be obtained by contacting the corresponding author.

REFERENCES

Aki, K., and P. G. Richards, 2002, Quantitative seismology, 2nd ed.: University Science Books.

Artman, B., I. Podladtchikov, and B. Witten, 2010, Source location using time-reverse imaging: Geophysical Prospecting, **58**, 861–873, doi: 10.1111/j.1365-2478.2010.00911.x.

Bao, X., and D. W. Eaton, 2016, Fault activation by hydraulic fracturing in western Canada: Science, **354**, 1406–1409, doi: 10.1126/science.aag2583.

Chambers, K., J. M. Kendall, S. Brandsberg-Dahl, and J. Rueda, 2010, Testing the ability of surface arrays to monitor microseismic activity: Geophysical Prospecting, **58**, 821–830, doi: 10.1111/j.1365-2478.2010.00893.x.

Claerbout, J., 1971, Toward a unified theory of reflection mapping: Geophysics, **36**, 467–481, doi: 10.1190/1.1440185.

Douma, J., R. Snieder, A. Fish, and P. Sava, 2013, Locating a microseismic event using deconvolution: 83th Annual International Meeting, SEG, Expanded Abstracts, 2206–2211, doi: 10.1190/segam2013-0446.1.

Drew, J., J. Zhang, and J. C. Le, 2014, The impact of channel count on microseismic event detection for a surface array: 84th Annual International Meeting, SEG, Expanded Abstracts, 2183–2187, doi: 10.1190/segam2014-1377.1.

Eaton, D. W., 2018, Passive seismic monitoring of induced seismicity: Fundamental principles and application to energy technologies: Cambridge University Press.

Eisner, L., P. M. Duncan, W. M. Heigl, and W. R. Keller, 2009, Uncertainties in passive seismic monitoring: The Leading Edge, **28**, 648–655, doi: 10.1190/1.3148403.

Fink, M., 2006, Time-reversal acoustics in complex environments: Geophysics, **71**, no. 4, SI151–SI164, doi: 10.1190/1.2215356.

Gajewski, D., and E. Tessmer, 2005, Reverse modelling for seismic event characterization: Geophysical Journal International, **163**, 276–284, doi: 10.1111/j.1365-246X.2005.02732.x.

Gao, W., M. Sacchi, and Z. Li, 2017, Microseismic-source location via elastic least-squares full-waveform inversion with a group sparsity constraint: 87th Annual International Meeting, SEG, Expanded Abstracts, 2814–2819, doi: 10.1190/segam2017-17785680.1.

Huang, J.-W., and B. Milkereit, 2007, Wave-equation-based separation of P- and S-wave modes: 77th Annual International Meeting, SEG, Expanded Abstracts, 2135–2139, doi: 10.1190/1.2792910.

Li, F., Y. Qin, and W. Song, 2019, Waveform inversion-assisted distributed reverse time migration for microseismic location: IEEE Journal of Selected Topics in Applied Earth Observations and Remote Sensing, **12**, no. 4, 327–332.

Li, J., H. Zhang, W. L. Rodi, and M. N. Toksoz, 2013, Joint microseismic location and anisotropic tomography using differential arrival times and differential backazimuths: Geophysical Journal International, **195**, 1917–1931, doi: 10.1093/gji/ggt358.

Li, Z., X. Ma, C. Fu, B. Gu, and G. Liang, 2015, Frequency-wavenumber implementation for P- and S-wave separation from multi-component seismic data: Exploration Geophysics, **47**, 32–43, doi: 10.1071/EG14047.

MacKay, S., and R. Abma, 1992, Imaging and velocity estimation with depth-focusing analysis: Geophysics, **57**, 1608–1622, doi: 10.1190/1.1443228.

Maxwell, S. C., J. Rutledge, R. Jones, and M. Fehler, 2010, Petroleum reservoir characterization using downhole microseismic monitoring: Geophysics, **75**, no. 5, 75A129–75A137, doi: 10.1190/1.3477966.

McMechan, G. A., 1982, Determination of source parameters by wavefield extrapolation: Geophysical Journal International, **71**, 613–628, doi: 10.1111/j.1365-246X.1982.tb02788.x.

Nakata, N., 2018, Extended imaging conditions for passive seismic data with GmRTM: 88th Annual International Meeting, SEG, Expanded Abstracts, 2957–2961, doi: 10.1190/segam2018-2998514.1.

Nakata, N., and G. C. Beroza, 2016, Reverse time migration for microseismic sources using the geometric mean as an imaging condition: Geophysics, **81**, no. 2, KS51–KS60, doi: 10.1190/geo2015-0278.1.

Poulin, A., R. Weir, D. Eaton, N. Igonin, Y. Chen, L. Lines, and D. Lawton, 2019, Focal-time analysis: A new method for stratigraphic depth control of microseismicity and induced seismic events: Geophysics, **84**, no. 6, KS173–KS182, doi: 10.1190/geo2019-0046.1.

Pujol, J., 2004, Earthquake location tutorial: Graphical approach and approximate epicentral location techniques: Seismological Research Letters, **75**, 63–74, doi: 10.1785/gssrl.75.1.63.

Sava, P., and S. Fomel, 2006, Time-shift imaging condition in seismic migration: Geophysics, **71**, no. 6, S209–S217, doi: 10.1190/1.2338824.

Schoenball, M., and W. L. Ellsworth, 2017, Waveform-relocated earthquake catalog for Oklahoma and southern Kansas illuminates the regional fault network: Seismological Research Letters, **88**, 1252–1258, doi: 10.1785/0220170083.

Schultz, R., R. Wang, Y. J. Gu, K. Haug, and G. Atkinson, 2017, A seismological overview of the induced earthquakes in the Duvernay play near Fox Creek, Alberta: Journal of Geophysical Research, Solid Earth, **122**, 492–505, doi: 10.1002/2016JB013570.

Schuster, G.T., J. Yu, J. Sheng, and J. Rickett, 2004, Interferometric/daylight seismic imaging: Geophysical Journal International, **157**, 838–852, doi: 10.1111/j.1365-246X.2004.02251.x.

Shapiro, S., 2015, Fluid-induced micro seismicity: Cambridge University Press.

Sharan, S., R. Wang, and F. J. Herrmann, 2018, Fast sparsity-promoting microseismic source estimation: Geophysical Journal International, **216**, no. 1, 164–181.

Skoumal, R. J., M. R. Brudzinski, and B. S. Currie, 2015, Earthquakes induced by hydraulic fracturing in Poland Township, Ohio: Bulletin of the Seismological Society of America, **105**, 189–197, doi: 10.1785/0120140168.

Song, C., T. Alkhalifah, and Z. Wu, 2019, Microseismic event estimation and velocity analysis based on a source-focusing function: Geophysics, **84**, no. 3, KS85–KS94, doi: 10.1190/geo2018-0205.1.

Sun, J., Z. Xue, S. Fomel, T. Zhu, and N. Nakata, 2016, Full-waveform inversion of passive seismic data for sources and velocities: 86th Annual International Meeting, SEG, Expanded Abstracts, 1405–1410, doi: 10.1190/segam2016-13959115.1.

Sun, J., T. Zhu, S. Fomel, and W. Song, 2015, Investigating the possibility of locating microseismic sources using distributed sensor networks: 85th Annual International Meeting, SEG, Expanded Abstracts, 2485–2490, doi: 10.1190/segam2015-5888848.1.

Sun, R., G. A. McMechan, H.-H. Hsiao, and J. Chow, 2004, Separating P- and S-waves in prestack 3D elastic seismograms using divergence and curl: Geophysics, **69**, 286–297, doi: 10.1190/1.1649396.

Thurber, C. H., and E. R. Engdahl, 2000, Advances in global seismic event location, *in* Advances in seismic event location, 3–22:Springer.

Virieux, J., 1984, SH-wave propagation in heterogeneous media: Velocity-stress finite-difference method: Geophysics, **49**, 1933–1942, doi: 10.1190/1.1441605.

Virieux, J., 1986, P-SV wave propagation in heterogeneous media: Velocity-stress finite-difference method: Geophysics, **51**, 889–901, doi: 10.1190/1.1442147.

Waldhauser, F., and W. L. Ellsworth, 2000, A double-difference earthquake location algorithm: Method and application to the northern Hayward fault, California: Bulletin of the Seismological Society of America, **90**, 1353–1368, doi: 10.1785/0120000006.

Wang, B., C. Mason, M. Guo, K. Yoon, J. Cai, J. Ji, and Z. Li, 2009, Subsalt velocity update and composite imaging using reverse-time-migration based delayed-imaging-time scan: Geophysics, **74**, no. 6, WCA159–WCA166, doi: 10.1190/1.3227152.

Wang, Y., S. C. Singh, and P. J. Barton, 2002, Separation of P- and SV-wavefields from multi-component seismic data in the τ-p domain: Geophysical Journal International, **151**, 663–672, doi: 10.1046/j.1365-246X.2002.01797.x.

Witten, B., and J. Shragge, 2015, Extended wave-equation imaging conditions for passive seismic data: Geophysics, **80**, no. 6, WC61–WC72, doi: 10.1190/geo2015-0046.1.

Witten, B., and J. Shragge, 2017, Image-domain velocity inversion and event location for microseismic monitoring: Geophysics, **82**, no. 5, KS71–KS83, doi: 10.1190/geo2016-0561.1.

Zhang, Z., J. Du, and F. Gao, 2018, Simultaneous inversion for microseismic event location and velocity model in Vaca Muerta Formation: Geophysics, **83**, no. 3, KS23–KS34, doi: 10.1190/geo2017-0010.1.

Zhang, Z., J. W. Rector, and M. J. Nava, 2017, Simultaneous inversion of multiple microseismic data for event locations and velocity model with Bayesian inference: Geophysics, **82**, no. 3, KS27–KS39, doi: 10.1190/geo2016-0158.1.

Zhu, J., L. Lines, and S. Gray, 1998, Smiles and frowns in migration/velocity analysis: Geophysics, **63**, 1200–1209, doi: 10.1190/1.1444420.

Zhu, T., J. Sun, D. Gei, J. M. Carcione, P. Cance, and C. Huang, 2019, Hybrid multiplicative time-reversal imaging reveals the evolution of microseismic events: Theory and field-data tests: Geophysics, **84**, no. 3, KS71–KS83, doi: 10.1190/geo2018-0662.1.